



## **Final Draft of the original manuscript**

Callegari, B.; Oliveira, J.; Coelho, R.; Brito, P.; Schell, N.; Soldera, F.; Mücklich, F.; Sadik, M.; Garcia, J.; Pinto, H.:

**New insights into the microstructural evolution of Ti-5Al-5Mo-5V-3Cr alloy during hot working.**

In: Materials Characterization. Vol. 162 (2020) 110180.

First published online by Elsevier: 04.02.2020

<https://dx.doi.org/10.1016/j.matchar.2020.110180>

## **New insights into the microstructural evolution of Ti-5Al-5Mo-5V-3Cr alloy during hot working**

Bruna Callegari<sup>a,b</sup>, João Pedro Oliveira<sup>c</sup>, Rodrigo S. Coelho<sup>d</sup>, Pedro P. Brito<sup>e</sup>, Norbert Schell<sup>f</sup>, Flavio Andrés Soldera<sup>b</sup>, Frank Mücklich<sup>b</sup>, M. Ibrahim Sadik<sup>g</sup>, Jose Luis Garcia<sup>g</sup>, Haroldo Cavalcanti Pinto<sup>a,\*</sup>

<sup>a</sup>University of São Paulo, São Carlos School of Engineering, Department of Materials Engineering, Av. João Dagnone 1100, 13563-120, São Carlos, Brazil

<sup>b</sup>Saarland University, Chair of Functional Materials, Campus 66123, Saarbrücken, Germany

<sup>c</sup>UNIDEMI, Department of Mechanical and Industrial Engineering, NOVA School of Science and Technology, NOVA University of Lisbon, 2829-516 Caparica, Portugal

<sup>d</sup>SENAI CIMATEC, Materials Science Department, Av. Orlando Gomes 1845, 41650-010, Salvador, Brazil

<sup>e</sup>Pontifical Catholic University of Minas Gerais, Av. Dom José Gaspar 500, 30535-901, Belo Horizonte, Brazil

<sup>f</sup>Institute of Materials Research, Helmholtz-Zentrum Geesthacht, Max-Planck-Str. 1, D-21502, Geesthacht, Germany

<sup>g</sup>Sandvik Machining Solutions, R&D Material & Processes, Lerkrogsvägen 19, SE 12160 Stockholm, Sweden

\*Corresponding author. Postal address: University of São Paulo, São Carlos School of Engineering, Department of Materials Engineering, Av. João Dagnone, 1100, 13563-120, São Carlos, SP, Brazil. E-mail address: haroldo@sc.usp.br. Telephone number: +55 16 33738290.

### **Highlights**

- Evidence of dynamic  $\alpha$  decomposition during deformation in the  $\alpha+\beta$  field.
- Different distributions of  $\alpha$  precipitates depending on the applied strain rate.
- Non-uniform recovery during deformation in the  $\beta$  field with a higher strain rate.
- Strong  $\beta$  texture and weak  $\alpha$  texture evaluated by XRD and misorientation analysis.

### **Abstract**

Microstructural features resulting from thermomechanical treatment of  $\beta$ -metastable Ti-5Al-5Mo-5V-3Cr (Ti-5553) alloy were studied by means of electron backscatter diffraction and X-ray diffraction. The alloy was deformed at 950°C ( $\beta$  field) and 800°C ( $\alpha+\beta$  field) with strain rates of 0.001 s<sup>-1</sup> and 0.1 s<sup>-1</sup> in compression mode up to a compression ratio of 0.5 (true ratio = 0.7). It was concluded that  $\beta$  undergoes dynamic recovery both above and below its  $\beta$ -transus temperature, and recovery is more dominant at lower strain rates, which was corroborated by EBSD misorientation measurements. Meanwhile,  $\alpha$  phase undergoes not only a process of breakage and globularization, but also decomposition, which contributes to flow softening. The increase in strain rate caused non-uniform recovery at 950°C and a more intense refinement of  $\alpha$  precipitates at 800°C. Macrotecture evaluation after deformation indicates that  $\beta$ 's texture is much stronger than that of  $\alpha$ , with its (200) component being the strongest one.

**Keywords:** Titanium alloys; Thermomechanical processing; Microstructure evolution; Electron backscattered diffraction; Synchrotron X-ray diffraction.

## 1. Introduction

The advantages of  $\beta$  titanium alloys arise from their excellent combination of physical and mechanical properties, generally including good corrosion properties too. Additionally, these alloys have good processability, which can be attained by a wide range of routes. According to Nyakana, Fanning and Boyer [1], one feature that makes  $\beta$ -type Ti alloys genuinely unique is the possibility of tuning their elastic modulus within a fairly wide range by altering processing parameters.

Ti-5Al-5Mo-5V-3Cr (Ti-5553) alloy, commercially known as TIMETAL® 555, is a high-strength  $\beta$  titanium alloy that was designed as an improved version of the Russian alloy VT22 (Ti-5Al-5Mo-5V-1Cr-1Fe). The alloy possesses better combination of strength, ductility, and toughness than VT22, and a final part can be achieved through more simplified processing approaches. According to Nyakana et al., the Ti-5553 alloy is capable of achieving strengths levels as high as 1517 MPa [1]. Besides improved processability and excellent mechanical properties, Ti-5553 alloy is also deeply hardenable [2]. As of 2005, the alloy was under evaluation to be employed in several major airframe components on new programs [1].

Ti-5553 is also frequently compared to Ti-10V-2Fe-3Al (Ti-1023), another widely used  $\beta$  alloy. Forging of both alloys is quite similar, but the higher  $\beta$ -transus of Ti-5553 enables forging operations in

the  $\alpha+\beta$  to be performed at temperatures approximately 56°C higher [2]. Another processing feature that differentiates both alloys is that, for Ti-5553, primary forging can be conducted either in the  $\beta$  or  $\alpha+\beta$  fields prior to the final  $\alpha+\beta$  forging [3]. Both routes can achieve similar strength levels, but primary  $\beta$  forging promotes higher ductility and fracture toughness [4]. Another difference between Ti-5553 and Ti-1023 is that the first one can be air cooled after ageing with no deterioration of properties, whereas the latter needs to be water quenched to obtain the same results [5]. According to Fanning and Boyer [4], this limits the section thickness of parts produced with Ti-1023 to 76 mm, while sections 152 mm thick are attainable in parts fabricated using Ti-5553. An additional advantage of Ti-5553 over Ti-2013 is that it exhibits a more robust processability. Typically, new suppliers of Ti-1023 forgings must go through a learning curve to attain the desired levels of strength, ductility and toughness, whereas Ti-5553's forging suppliers have been able to supply products which meet the requirements at their first attempt. Similarly to Ti-1023, its highest recommended service temperature is around 315°C [1].

Several works have been developed in order to understand Ti-5553 alloy's response to thermomechanical processing in terms of microstructural evolution and resulting mechanical properties. Jones et al. [5] have proposed that the initial flow behavior and the dominating deformation mechanism of the alloy depends on the morphology and fraction of  $\alpha$  precipitates. They have also suggested that the flow softening observed is caused by the fragmentation of high aspect ratio  $\alpha$  laths due to local strains resulting from the accumulation of dislocations. However, they have pointed out that the volume fraction of grain boundary  $\alpha$ , for example, also affects the flow softening, but have not evaluated this contribution. Jones and Jackson [6] have reinforced that  $\alpha$  plates become fragmented during the forging process and, depending on strain rate, they can transform into a well distributed globular microstructure. They also show that adiabatic heating effects are minimal during forging of small samples at low strain rates, thus attributing the flow softening solely to the fragmentation of  $\alpha$  platelets. Finally, they have also confirmed what had been suggested in previous studies regarding accumulation of dislocations surrounding  $\alpha$  platelets and their resulting role as barriers to deformation. Matsumoto et al. [7] have tested the alloy in a wide range of temperatures and deformation rates. They affirm that the behavior of stress-strain curves, with continuous flow softening at lower temperatures and higher strain rates and with achievement of a steady state at higher temperatures and lower strain rates, indicates that dynamic recovery becomes dominant with increasing temperature and decreasing strain rate, which has been corroborated by the calculation of activation energies of  $\beta$  phase deformation. In microstructures deformed at and above

800°C, they proposed the activation of continuous dynamic recrystallization in the vicinity of prior  $\beta$  grain boundaries at lower strain rates. There appears to be a general agreement that dynamic recovery of  $\beta$  phase governs deformation, and that the main softening mechanism is due to break-up and globularization of the  $\alpha$  phase. This has also been proposed for Ti-1023 alloy [8,9]. Poletti et al. [10] also attribute softening to the coarsening of  $\beta$  subgrains.

A relevant aspect of studying the deformation behavior of  $\beta$  alloys arises from the need of understanding how deformation affects subsequent heat treatments, given that these alloys generally undergo ageing treatments to promote strengthening by precipitation of a refined  $\alpha$  phase. It is well known that  $\beta$  alloys need nucleation sites to allow for  $\alpha$  precipitation during ageing [11]. In this context, lattice defects such as dislocations and low-angle grain boundaries (LAGBs) may act as additional nucleation sites for phase precipitation. Furuhashi and Maki have reported on the crystallography of heterogeneous nucleation on defects during phase transformations in  $\beta$  titanium alloys and ferrous alloys, and have pointed out the role of dislocations and sub-grain boundaries as preferential nucleation sites [12]. This role has been reinforced in the review of Kolli and Devaraj on metastable  $\beta$  titanium alloys [13]. Teixeira et al. have modelled the effect of  $\beta$  phase plastic deformation on  $\alpha$  precipitation during subsequent cooling and proposed that LAGBs act as nucleation sites for grain boundary  $\alpha$  ( $\alpha_{GB}$ ) allotriomorph. They have also assessed the likeliness of Widmanstätten  $\alpha$  colonies growth from  $\alpha_{GB}$  ( $\alpha_{WGB}$ ) [14]. In a later work also involving modelling of  $\alpha$  precipitation as influenced by deformation of the  $\beta$  phase, the same authors highlighted the importance of accurate information on the misorientation distributions of the  $\beta$  phase for the success of the developed model [15].

The present work presents a study on the microstructural evolution of  $\beta$ -metastable alloy Ti-5553 subjected to deformation at different strain rates both at  $\beta$  and  $\alpha+\beta$  fields starting from a fully  $\beta$  condition. It complements works previously developed on the subject, providing a macrotexture evaluation following deformation and evidences of the occurrence of phenomena such as non-uniform recovery and dynamic phase transformation, as well as relying on high energy X-ray diffraction as an additional tool to study the effects of deformation on the microstructure.

## **2. Materials and methods**

### **2.1. Material**

The composition of Ti-5553 alloy used in this work is given in **Table 1**. Amounts of heavier elements, i.e. Al, Mo, V, Cr and Fe, were measured by inductively coupled plasma – atomic emission spectrometry using an Ametek® SPECTROMAXx analyzer. Oxygen amount was analyzed via inert gas fusion using a Leco® RO-400 analyzer; nitrogen and hydrogen were analyzed with a Leco® ONH-836 equipment; and carbon was analyzed in a Leco® CS-844 analyzer. Its  $\beta$ -transus temperature, measured by differential scanning calorimetry in a Netzsch® 404 F3 Pegasus calorimeter with heating rate of 20°C/min, is of approximately 875°C. The as-received alloy presented the bimodal microstructure shown in **Figure 1**, which comprises the  $\alpha$  phase with globular morphology (primary  $\alpha$ ,  $\alpha_p$ ) and lamellar morphology (secondary  $\alpha$ ,  $\alpha_s$ ) within a  $\beta$  matrix. It is also possible to observe some remaining  $\alpha$  phase at prior  $\beta$  grain boundaries ( $\alpha_{GB}$ ).

Element	Ti	Al	Mo	V	Cr	Fe	O	C	N	H
wt%	Bal.	5.36	4.42	5.01	2.93	0.48	0.16	0.03	0.005	0.002
[Al]eq		6.9			[Mo]eq			12.6		

**Table 1.** Composition of Ti-5553 alloy used in this work.

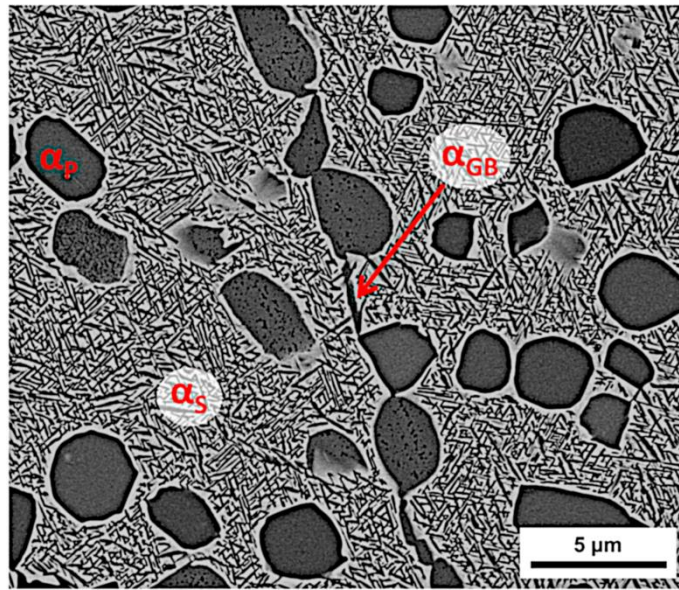


**Figure 1.** Bimodal microstructure of the as-received Ti-5553 alloy with indication of the different  $\alpha$  morphologies:  $\alpha_p$ ,  $\alpha_s$  and  $\alpha_{GB}$ .

## 2.2. Thermomechanical treatments

The Ti-5553 alloy was thermomechanically treated by means of uniaxial compression at 950°C ( $\beta$  field) and 800°C ( $\alpha+\beta$  field). Specimens with dimensions of  $\phi 10 \times 15$  mm were cut from the as-

received bar with their length parallel to the bar's length. To remove any effects of prior processing, specimens initially underwent a homogenization treatment at 950°C during 30 minutes followed by water quenching in an EDG 10P-S furnace with vacuum and argon atmosphere protection. Compressions were imposed in a Gleeble® 3800 thermomechanical simulator with strain rates of  $10^{-1} \text{ s}^{-1}$  and  $10^{-3} \text{ s}^{-1}$  up to a compression ratio of 50% (true strain = 0.7). The alloy was also heat-treated at 800°C without deformation for microstructural comparison between heat-treated and deformed conditions. **Figure 2** represents schematically the framework of treatments imposed to the alloy as well as the names given to each condition based on the temperature (“950C” for 950°C and “800C” for 800°C) and type (“HT” for heat treatment and “D1” and “D001” for compressions with strain rates of  $10^{-1}$  or 0.1 and  $10^{-3}$  or 0.001  $\text{s}^{-1}$ , respectively).

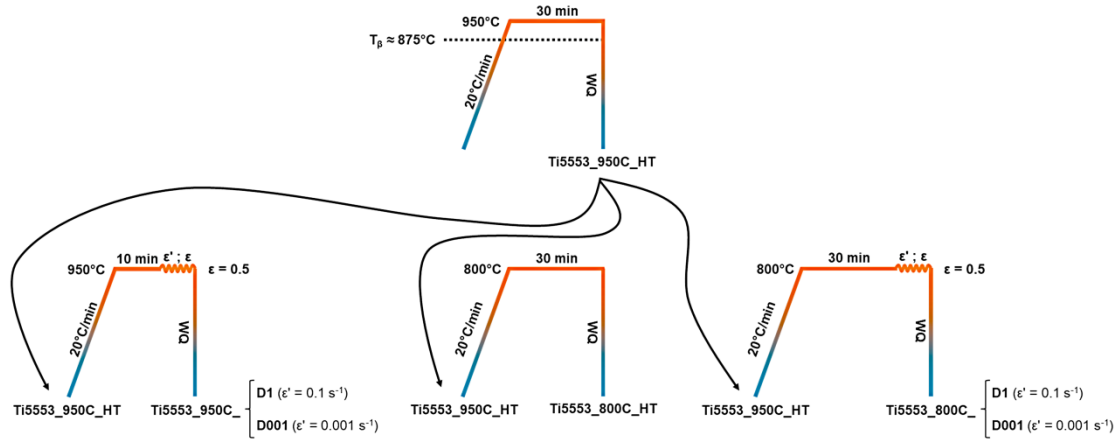


**Figure 2.** Schematic representation of thermomechanical and heat treatments imposed to Ti-5553 alloy.

### 2.3. Microstructural characterization

The alloy was metallographically prepared for light optical microscopy (LOM) and scanning electron microscopy (SEM) according to the following procedure: manual grinding steps using #320, #600 and #1200 sandpapers, automated pre-polishing with a 3  $\mu\text{m}$  diamond suspension and final automated polishing using a solution composed by 90 vol% 0.04  $\mu\text{m}$  OP-S and 10 vol%  $\text{H}_2\text{O}_2$ . Automated steps were carried out in a Buehler® EcoMet 250 machine (force: 5N; base rotation: 20 rpm; head rotation: 60 rpm; counter-rotation). For the electron backscattered diffraction analyses (EBSD), the alloy was prepared following the same steps using a TegraPol-21 machine (force: 10 N; base rotation: 50 rpm; head rotation: 50 rpm; both rotations in the same direction). A final light manual polishing with the OP-S

– H<sub>2</sub>O<sub>2</sub> solution during 5 minutes was added to ensure the removal of residual scratches from the surface. Samples were not chemically etched for microscopy.

LOM analyses were done in a Zeiss® Axio Scope.A1 optical microscope. SEM analyses were carried out in a FEI® Inspect F50 microscope with field emission gun using backscattered electrons' (BSE) signal. EBSD analyses were conducted in a FEI® Helios NanoLab 600 microscope also equipped with field emission gun. Step sizes were 1 μm for maps with lower magnification and 200 nm for maps with higher magnification. In the case of compressed specimens, all images were done on the plane parallel to the compression axis.

#### **2.4. Texture analysis**

To evaluate the macrotexture evolution upon deformation, pole figures of (110) $\beta$ , (200) $\beta$  and (211) $\beta$  reflections were measured for all deformed specimens. In the case of specimens deformed in the  $\alpha+\beta$  field, pole figures of (0002) $\alpha$ , (10 $\bar{1}$ 0) $\alpha$ , (10 $\bar{1}$ 1) $\alpha$ , (10 $\bar{1}$ 2) $\alpha$  and (11 $\bar{2}$ 0) $\alpha$  reflections were also measured. Orientation distribution functions (ODFs) were calculated using all reflections and pole figures were recalculated from calculated ODFs. Calculations were carried out using the MTEX toolbox for MATLAB® [16]. Measurements were done in a PANalytical® Empyrean X-ray diffractometer using Cu K $\alpha$  ( $\lambda = 1.54 \text{ \AA}$ ) radiation. The step size for both  $\varphi$  (0 – 360°) and  $\psi$  (0 – 85°) coordinates was 5°. In this case, measurements were done on the surface normal to the compression axis, which was polished following the same procedure adopted for EBSD analyses described in section 2.3.

#### **2.5. Synchrotron high energy X-ray diffraction**

Produced conditions were analyzed using synchrotron high energy X-ray diffraction (HEXRD). Samples with 3 × 4 × 6 mm were wire cut from the specimens. In the case of deformed conditions, samples were cut with their length parallel to the compression axis. Experiments were done in the P07B beamline of the PETRA III facility at DESY (Hamburg, Germany). The energy of the beam was 87.1 keV ( $\lambda = 0.142 \text{ \AA}$ ). Complete Debye-Scherrer rings were acquired in transmission mode using a Perkin Elmer® 2D fast detector with 200 × 200 μm<sup>2</sup> pixel size. An exposure time of 0.2 s was used, and 5 frames/image were acquired using a spot size of 1 × 1 mm<sup>2</sup>. Acquired images were treated using ImageJ software to obtain the corresponding diffractograms.

Quantitative analyses were carried out on PeakFit and MAUD [17] softwares to obtain parameters such as phase fractions and width and area of peaks. The calculation of peak parameters on PeakFit was done using a combined Gauss+Lorentz profile and Rietveld refinement was done on MAUD after instrument calibration using a standard LaB<sub>6</sub> powder.

### 3. Results

**Figure 3** depicts the microstructures resulting from heat treatments and deformation. For specimens heat-treated and deformed at 950°C, only LOM images are shown because the microstructure was composed solely by  $\beta$  phase grains. Note that no precipitates were detectable even by SEM. It is possible to observe that both Ti5553\_950HT and Ti5553\_800HT samples present a microstructure composed by equiaxed  $\beta$  grains. In the case of the Ti5553\_800HT sample, a considerable amount of  $\alpha$  phase is present both within grains and along grain boundaries. On the other hand, deformed conditions present elongated  $\beta$  grains with their longer axis normal to the compression direction. With respect to the presence of the  $\alpha$  phase, a significantly lower amount is present in comparison to the heat treated condition. Moreover, comparing both deformed conditions, Ti5553\_800C\_D001 presents coarser  $\alpha$  precipitates, with approximately the same size as those seen dispersed within  $\beta$  grains in Ti5553\_800HT condition.

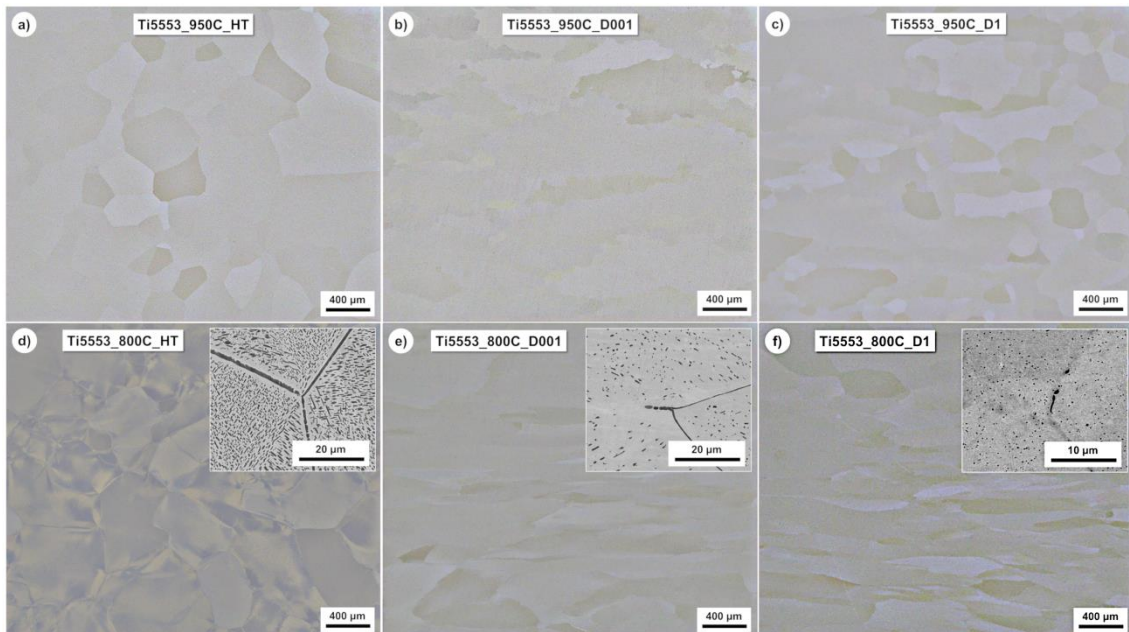


**Figure 3.** Microstructures of **a)** Ti5553\_950C\_HT (LOM), **b)** Ti5553\_950C\_D001 (LOM), **c)** Ti5553\_950C\_D1 (LOM), **d)** Ti5553\_800C\_HT (LOM with a BSE-SEM image in the inset), **e)** Ti5553\_800C\_D001 (LOM with a BSE-SEM image in the inset) and **f)** Ti5553\_800C\_D1 (LOM with a

BSE-SEM image in the inset). The compression axis is parallel to the height of images. The dark phase is  $\alpha$  and the bright phase is  $\beta$ .

**Figure 4** presents the flow curves of Ti-5553 alloy upon deformation at both temperatures and deformation rates. As expected, the lower the temperature and the higher the strain rate, the higher the peak stress. Also, in all cases it is possible to observe a steady state after the peak curve, without significant softening, indicating the dominance of dynamic recovery over recrystallization, especially during deformation in the  $\beta$  field. The occurrence of softening during compression in the  $\alpha+\beta$  field further confirms that  $\beta$  phase undergoes solely dynamic recovery. Softening is thus attributed to the change in morphology of the  $\alpha$  phase, i.e. its break-up and globularization. This is evidenced in this Ti-5553 alloy and also in other  $\beta$  alloys, such as Ti-1023, where  $\alpha$  laths break up into a necklace of small  $\alpha$  particles [8]. Jones and Jackson [6] have proposed that, during forging of Ti-5553 alloy with acicular  $\alpha$  precipitates, the initial work hardening up to the peak stress is dominated by the pile-up of dislocation at  $\alpha$  particles causing work hardening to a peak stress, point at which the local strain is sufficient to trigger the fragmentation of  $\alpha$  phase, removing dislocation barriers and causing the flow stress drop.

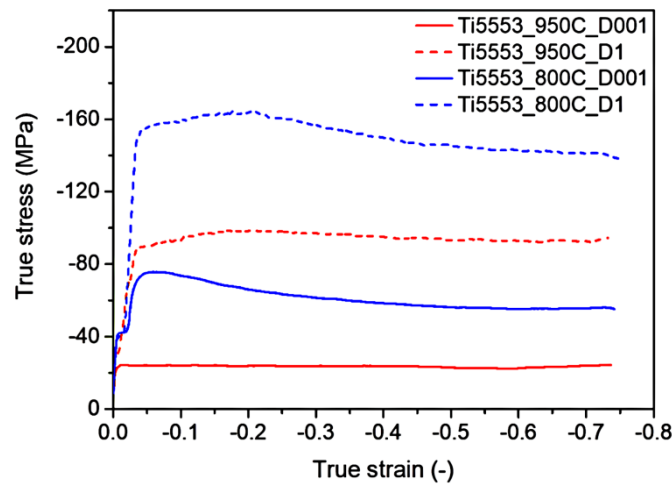


**Figure 4.** Flow curves of Ti-5553 alloy upon uniaxial compression at 950°C and 800°C with strain rates of 0.001 s<sup>-1</sup> and 0.1 s<sup>-1</sup>.

Due to microstructural coarseness, a conventional XRD macrotexture analysis was carried out in order to maximize the probed area, hence increasing the amount of probed grains and consequently improving statistics for texture evaluation. **Figure 5** presents the calculated pole figures for Ti-5553 alloy deformed at 950°C. It is possible to notice that (110) $\beta$  texture does not vary significantly between both

strain rates and is not expressive in neither of both cases, presenting the expected fiber texture with its highest intensity around  $\psi = 45^\circ$ . However,  $(200)\beta$  and  $(211)\beta$  textures vary considerable between both strain rates. The first is much more intense in Ti5553\_950C\_D001 with a strong fiber component, whereas it presents itself weaker in Ti5553\_950C\_D1, with the appearance of three additional poles around  $\psi = 60^\circ$ . The latter does not present intensity variation between both strain rates, but, in a similar manner as for  $(200)\beta$  reflection, it presents three additional poles at lower  $\psi$  values. The stronger  $(200)$  texture is in good agreement with previous works showing the strengthening of  $\langle 100 \rangle$  fiber texture with decreasing strain rate in  $\beta$  alloys [18]. The formation of a strong  $\langle 100 \rangle$  texture at low strain rates during compression is mainly attributed to dynamic strain-induced boundary migration, as proposed by Li et al for the deformation of a Ti-5Al-5Mo-5V-1Cr-1Fe alloy [19].

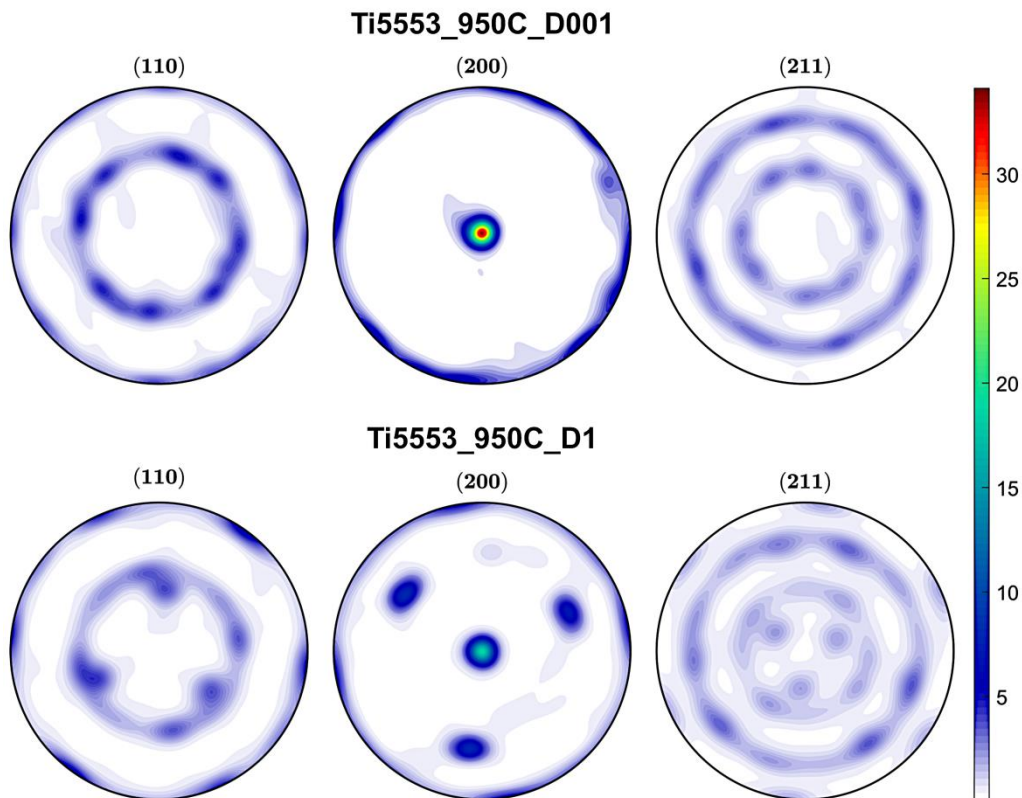


**Figure 5.** Calculated pole figures of  $(110)\beta$ ,  $(200)\beta$  and  $(211)\beta$  reflections of Ti-5553 alloy deformed at  $950^\circ\text{C}$ .

**Figure 6** depicts the calculated pole figures of  $\alpha$  and  $\beta$  reflections for when the material was deformed at  $800^\circ\text{C}$ . No significant texture differences can be seen in the  $\alpha$  phase with variation of strain rate. The most noticeable difference occurs for the  $(0002)\alpha$  reflection, which presents a more defined fiber texture in Ti5553\_800C\_D001. With respect to the  $\beta$  phase, the most noticeable difference is seen

between  $(200)\beta$  reflections, being the texture in the Ti5553\_800C\_D1 condition weakened, in a similar manner as for deformation in the single  $\beta$  field. In comparison with samples deformed at  $950^\circ\text{C}$ , the texture of  $\beta$  is weakened. It is interesting to notice the difference in intensity distributions of  $(0002)\alpha$  and  $(110)\beta$  pole figures in both conditions, given by the well-defined fiber aspect of the  $(110)\beta$  texture that is not strictly accompanied by the  $(0002)\alpha$  texture, which shows slight deviations from Burgers orientation relationship (BOR)  $\{0001\}\alpha\|\{110\}\beta$  between  $\alpha$  and  $\beta$  phases. Such deviations from the BOR after hot deformation have been observed in other alloys, such as Ti-7Mo-3Al-3Nb-3Cr [20] and Ti-5Al-5Mo-5V-1Cr-1Fe [21].

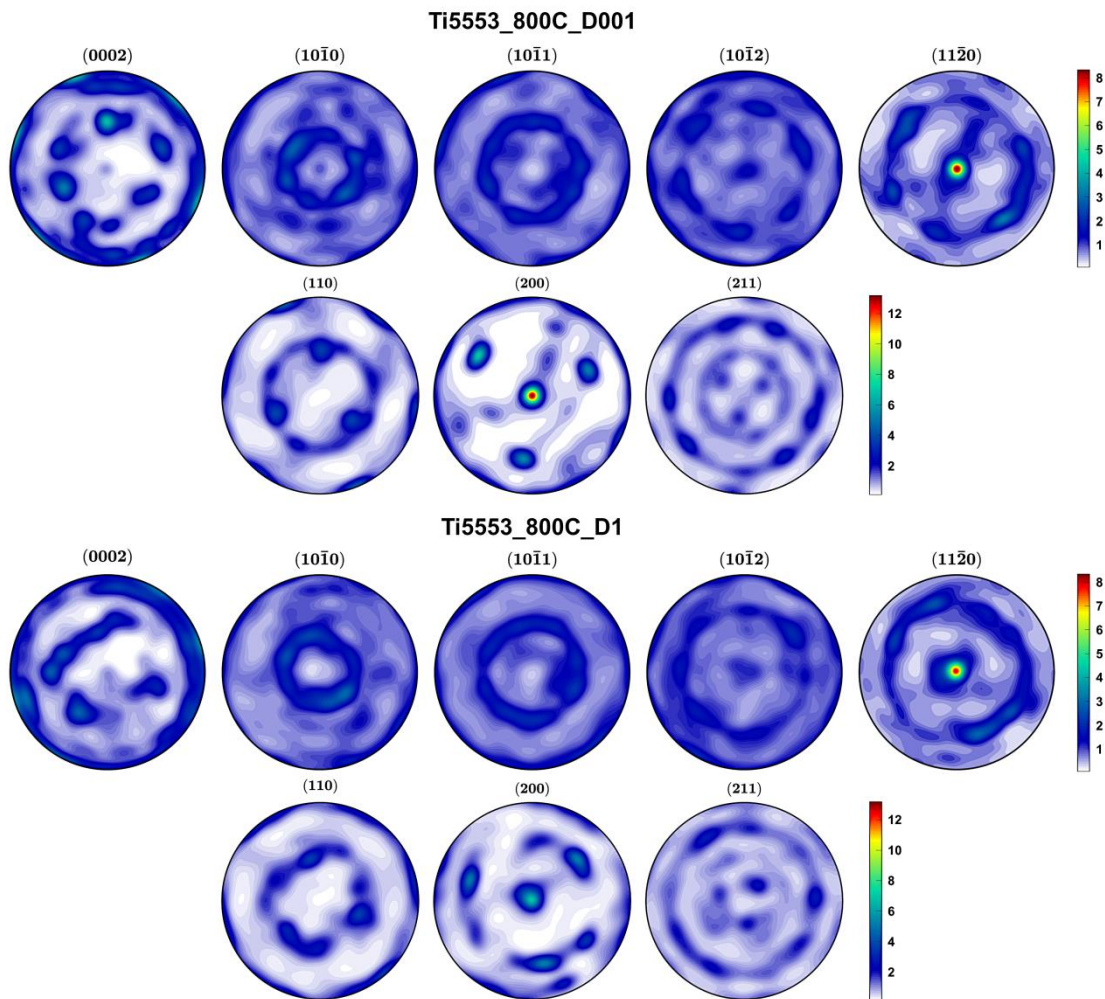


**Figure 6.** Calculated pole figures of  $(0002)\alpha$ ,  $(10\bar{1}0)\alpha$ ,  $(10\bar{1}1)\alpha$ ,  $(10\bar{1}2)\alpha$  and  $(11\bar{2}0)\alpha$ ,  $(110)\beta$ ,  $(200)\beta$  and  $(211)\beta$  reflections of Ti-5553 alloy deformed at  $800^\circ\text{C}$ .

## 4. Discussion

### 4.1. Processing in the single $\beta$ field

**Figure 7** shows the inverse pole figures (IPF) of the Ti-5553 alloy deformed at 950°C. The compression direction lies in the vertical axis for all images. Additionally, are shown plots of grain boundaries with indication of misorientation angles in **Figure 7b** and **Figure 7e**. A misorientation angle of 15° was defined as the threshold to separate high-angle (HAB) and low-angle boundaries (LAB). In addition, it is possible to observe regions with different orientations inside prior grains in **Figure 7a** and **Figure 7d**, which indicate the presence of subgrains whose boundaries have not been outlined. Since the minimum software-defined threshold angle defined to identify boundaries is of 2°, the non-indexed regions represent boundaries with a misorientation lower than 2°, i.e. in the early stages of recovery. These are more clearly seen in the Kernel average misorientation (KAM) maps in **Figure 7c** and **Figure 7f**. Kernel average misorientation is useful to analyze dislocation density, being areas with low KAM values (blue) the leanest in dislocations and areas with high KAM values (red) the richest in dislocations [22]. As expected, the highest dislocation densities are concentrated along boundaries, and it is possible to observe that the average KAM is higher in the sample deformed with a higher rate. Given the absence of refined grains with high angle boundaries, no evidence of dynamic recrystallization was found. In Ti5553\_950C\_D1, it is also possible to observe coarse prior  $\beta$  grains without any apparent substructure formation, indicated by the arrows in **Figure 7d**, which can also be seen in **Figure 3c**. This non-uniform microstructure has been observed in the  $\beta$ -metastable Ti-5Al-5Mo-5V-1Cr-1Fe titanium alloy after recrystallization in the  $\beta$  field following an  $\alpha+\beta$  forging [23]. The difference in formation of substructures, which would form new grains with high angle boundaries during a subsequent recrystallization treatment, is given by the difference in interfacial energy of grains as function of their crystallographic orientation. During recrystallization, substructured grains can either evolve or be consumed by non-substructured grains. It is a phenomenon to be considered, since this heterogeneous restoration leads to a heterogeneous microstructure, which can be deleterious for the mechanical properties of the material.

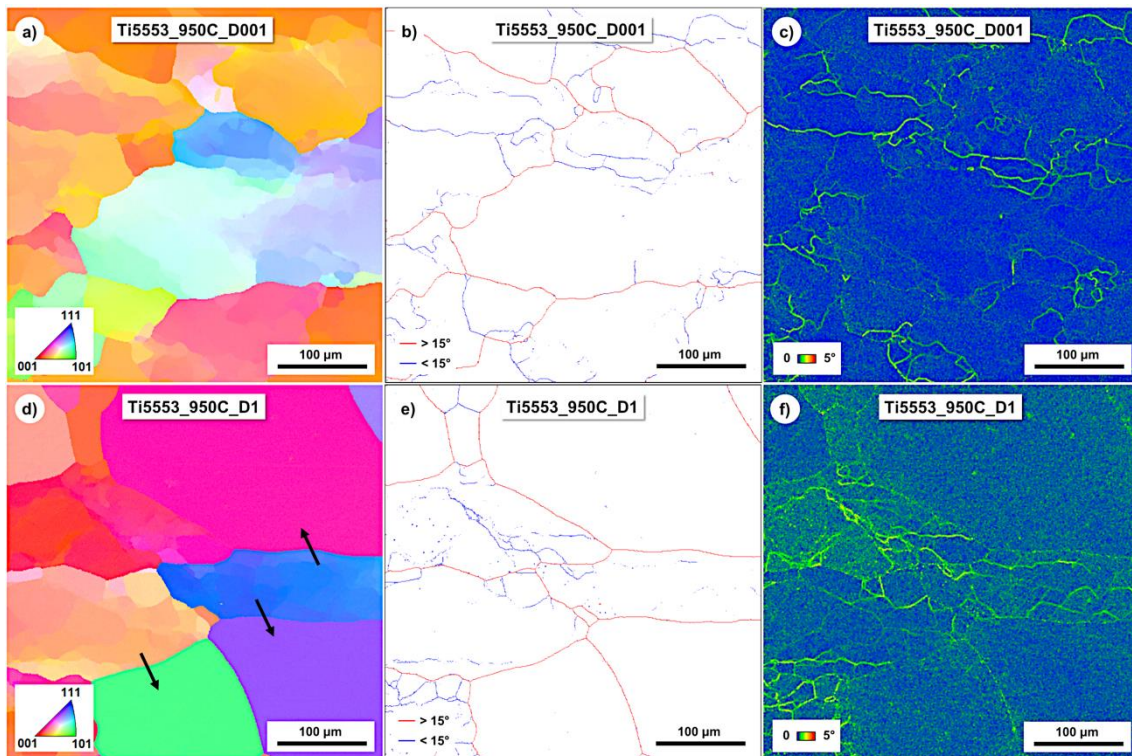


**Figure 7.** a) IPF, b) grain boundary and c) Kernel average misorientation maps of Ti5553\_950C\_D001 condition and d) IPF, e) grain boundary and f) Kernel average misorientation maps of Ti5553\_950C\_D1 condition. The compression axis is parallel to the height of images.

The misorientation distribution of the  $\beta$  phase for both deformed conditions is given in **Figure 8**. A higher fraction of low angle misorientations is seen in Ti5553\_950C\_D001, in accordance to the calculation of LABs' fractions carried out based on Figure 7b and Figure 7e, which yielded values of 48.9% for Ti5553\_950C\_D1 and 56.4% for Ti5553\_950C\_D001. This indicates the intensification of dynamic recovery with the reduction of strain rate. These results go against those typically observed during hot working of  $\beta$  titanium alloys in the  $\beta$  field, with the dominance of dynamic recovery at higher strain rates [7,18,24]. This can be explained by the heterogeneous deformation of grains that has already been discussed for **Figure 7**. Not all grains have experienced the formation of substructures and therefore the resulting fraction of LABs is lower.

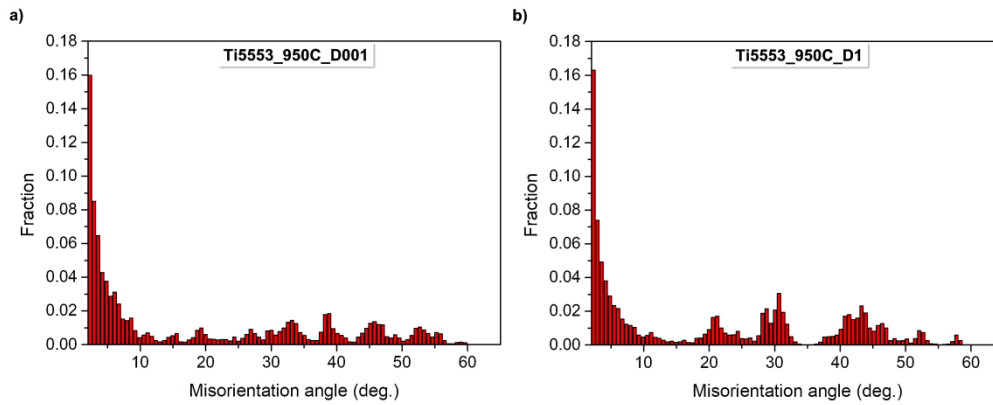


**Figure 8.** Misorientation distributions of  $\beta$  phase in a) Ti5553\_950C\_D001 and b) Ti5553\_950C\_D1 conditions.

#### 4.2. Processing in the $\alpha+\beta$ field

**Figure 9** shows the IPF maps of Ti-5553 alloy deformed at 800°C. Due to the coarse step size used in comparison to the size of  $\alpha$  precipitates as seen in SEM images (see **Figure 3**), smaller areas were chosen within the larger maps to be scanned with a finer step size. In these conditions, it is possible to observe that  $\alpha$  precipitates are more homogeneously distributed within the  $\beta$  matrix and also on grain boundaries in Ti5553\_800C\_D001 condition, whereas for Ti5553\_800C\_D1 condition it is highly concentrated along grain boundaries, being present in a much lower amount inside  $\beta$  grains. Also, the Ti5553\_800C\_D001 sample shows a typical feature of dynamic recovery: elongated grains with serrated primary boundaries. Additionally, one can notice the degree of fragmentation of  $\alpha$  particles upon faster deformation. Finally, it is also possible to notice a more intense substructure formation within prior  $\beta$  grain sizes with resulting coarser sub-grains in the slowly deformed condition in comparison with the one deformed with higher strain rate, in which the formation of finer sub-grains is more restricted to the boundaries of prior  $\beta$  grains. The distribution characteristic of  $\alpha$  phase seen in this work after deformation in the  $\alpha+\beta$  field further exemplifies the role of boundaries on the preferred precipitation of  $\alpha$  [20,25].

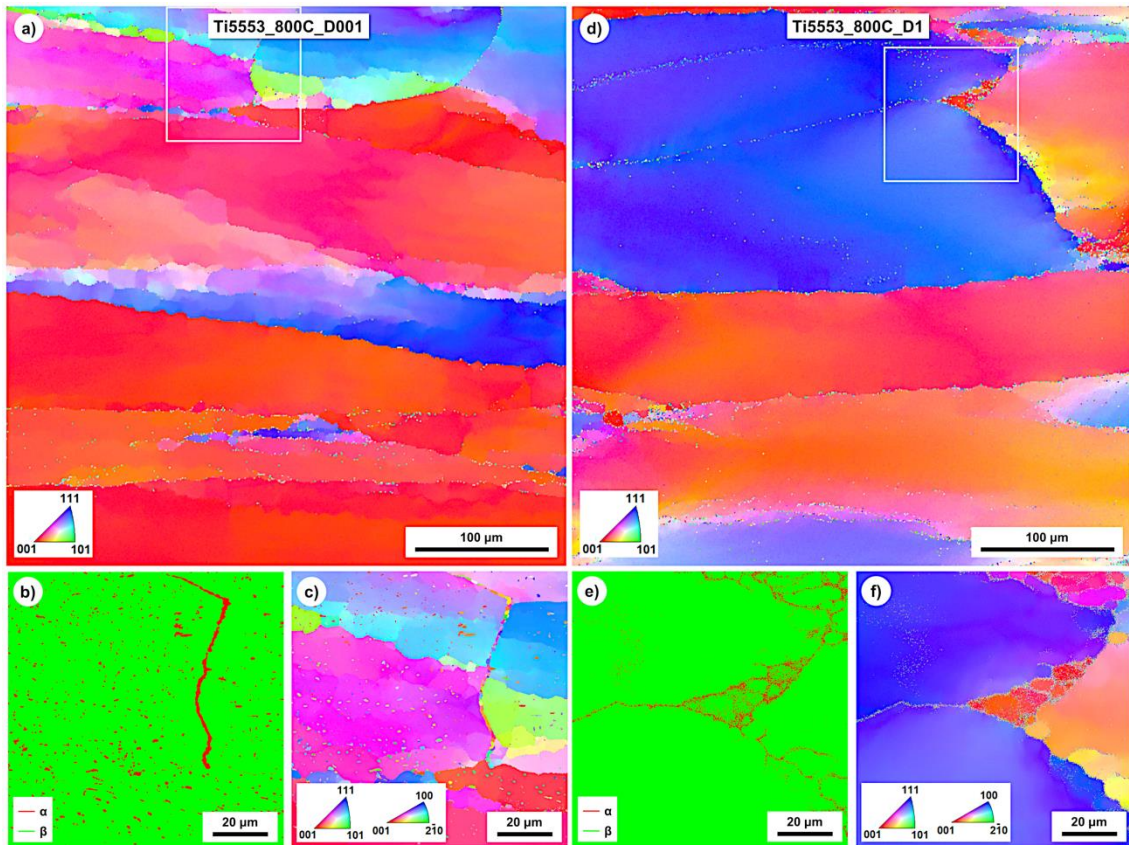


**Figure 9.** **a)** Low magnification IPF, **b)** high magnification phase map and **c)** high magnification IPF of Ti5553\_800C\_D001 condition and **d)** low magnification IPF, **e)** high magnification phase map and **f)** high magnification IPF of Ti5553\_800C\_D1 condition. The white squares in indicate the chosen areas for the higher magnification mapping, and compression axis is parallel to the height of images.

#### 4.2.1. Behavior of $\beta$ phase

The substructure distribution can be seen more clearly in the maps of grain boundaries for both conditions shown in **Figure 10a** and **Figure 10b**, whose threshold was defined in the same manner as for conditions deformed at 950°C. Fractions of LABs for Ti5553\_800C\_D001 and Ti5553\_800C\_D1 were 44.0% and 37.6%, respectively. Here, again, it is possible to observe regions with different orientations that indicate the presence of sub-grains whose boundaries were not indexed. These also correspond to boundaries in the early stages of recovery with a misorientation lower than 2°. In Ti5553\_800C\_D001, it is also possible to notice the presence of recrystallized grains decorating prior  $\beta$  grain boundaries in a necklace structure, indicating the occurrence of discontinuous dynamic recrystallization as well [26]. The Kernel average misorientation maps of each condition are shown in **Figure 10c** and **Figure 10d**. Again, the rapidly deformed condition presents a higher dislocation density and therefore a higher KAM value. In comparison to conditions deformed at 950°C, the average KAM is higher, being the highest values

concentrated in boundaries with the presence of  $\alpha$ , indicating a higher dislocation density in the vicinities of  $\alpha$  precipitates.

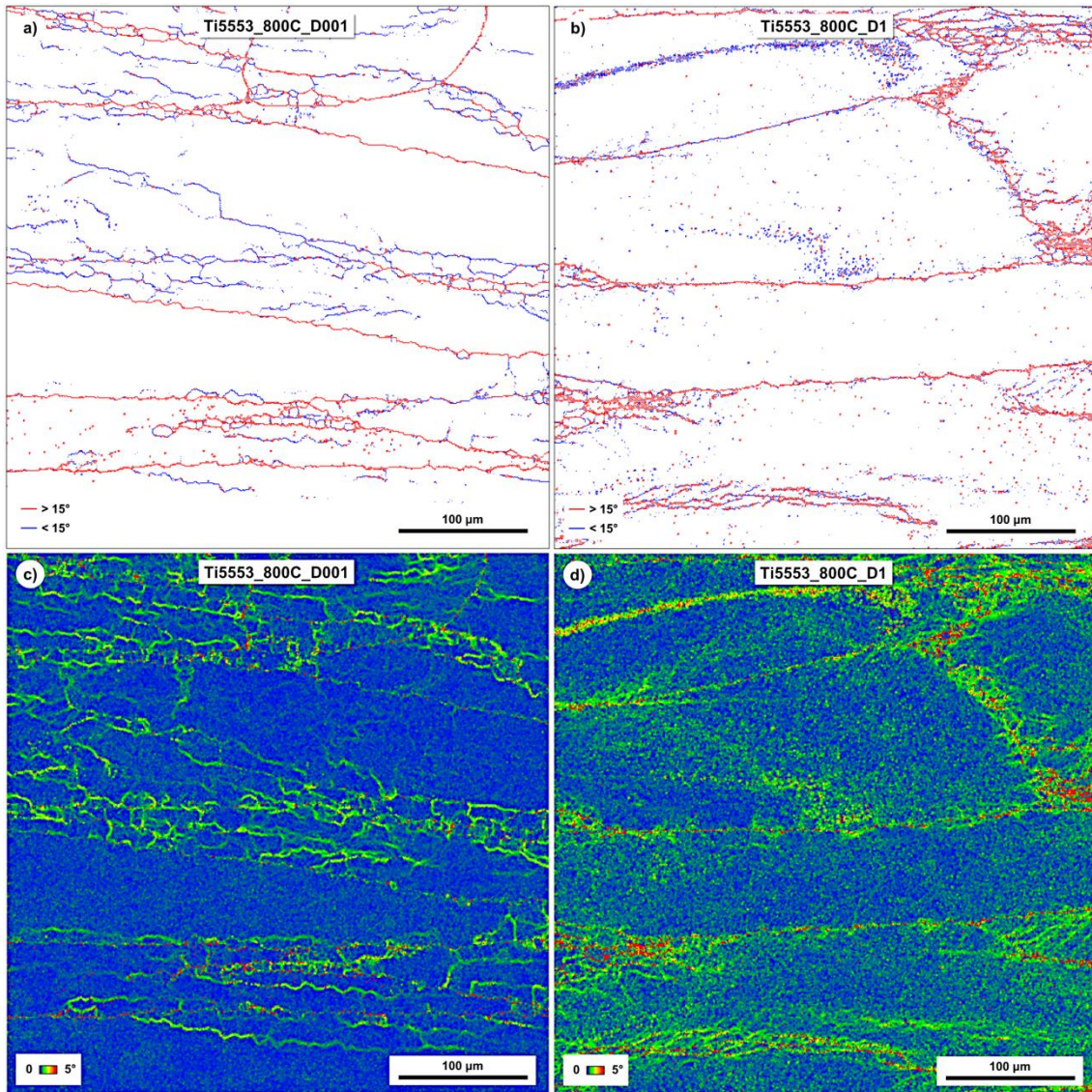


**Figure 10.** Grain boundary maps of **a)** Ti5553\_800C\_D001 and **b)** Ti5553\_800C\_D1 conditions and Kernel average misorientation maps of **c)** Ti5553\_800C\_D001 and **d)** Ti5553\_800C\_D1 conditions. The compression axis is parallel to the height of images.

**Figure 11** summarizes the misorientation distribution of  $\beta$  phase for the conditions deformed at 800°C. In this case, the higher fraction of low angle misorientations is evident, indicating that in the dual phase field, dynamic recovery becomes dominant with decreasing strain rate [7].

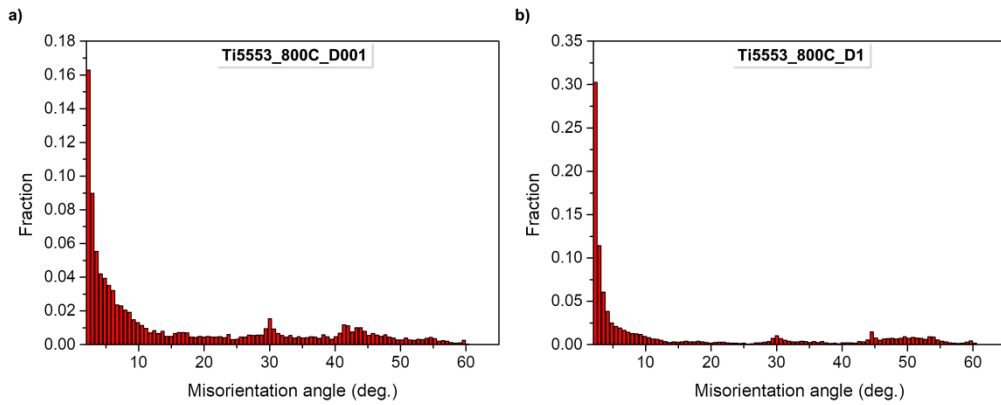


**Figure 11.** Misorientation distribution of  $\beta$  for a) Ti5553\_800C\_D001 and b) Ti5553\_800C\_D1 conditions.

#### 4.2.2. Fragmentation and decomposition of $\alpha$ phase during deformation

As seen in the SEM insets in **Figure 3**, the amount of  $\alpha$  phase has decreased considerably in both deformed conditions with respect to the heat-treated condition. **Figure 12** presents the temperature read by thermocouples during treatment, where a slight temperature variation of  $\pm 7^\circ\text{C}$  can be seen. Earlier studies have shown that adiabatic heating effects are negligible when forging small samples at strain rates of the order of the ones used in this study [6]. This demonstrates that a dynamic decomposition of  $\alpha$  phase occurs, presenting itself as an additional softening mechanism. These findings go against those from Jones et al. [27] during thermomechanical processing of the same alloy with an initial microstructure composed by globular  $\alpha$  dispersed in a  $\beta$  matrix, in which the initial globular  $\alpha$  morphology was maintained with little or no alteration, and the  $\alpha$  size distribution showed almost no deviation among strain rates, indicating there was no effect of strain rate on particle size. On the other hand, it agrees well with the results from Matsumoto et al. [7], who observed a decrease in  $\alpha$  fraction with the increase of strain rate. Nonetheless, Matsumoto et al. propose a dynamic precipitation of  $\alpha$ , with an increase in precipitation with the decrease in strain rate, and the present results show that what occurs, in fact, is a dynamic decomposition of  $\alpha$  into  $\beta$  that intensifies with the increase in strain rate.

The dissolution of  $\alpha$  during deformation has been observed for Ti-5553 [10,28] and Ti-5Al-5Mo-5V-3Cr-1Zr (Ti-55531) [29] alloys at moderate strain rates. In the latter,  $\alpha$  dissolution at low strain rates is attributed to a modification of equilibrium conditions due to deformation or to a non-equilibrium condition of the alloy before deformation. However, because the volume fraction of  $\alpha$  is even lower after deformation at higher strain rate, dissolution due to the aforementioned adiabatic heating might be a hypothesis. However, thermodynamic simulations are necessary to confirm this assumption.

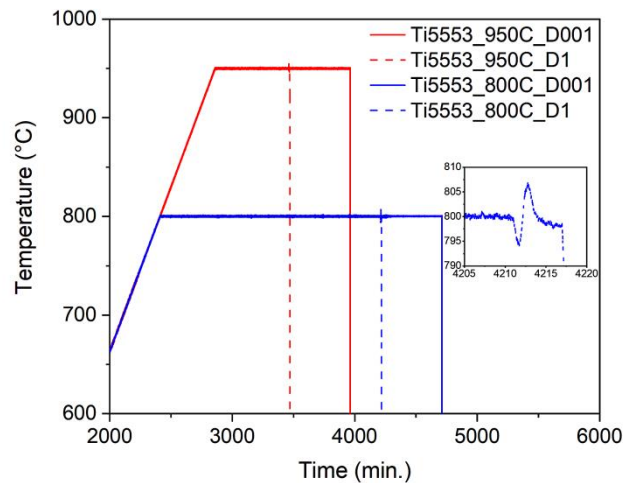


**Figure 12.** Temperature evolution during treatments with an inset showing temperature variation during deformation of Ti5553\_800C\_D1 condition.

Given the difference between the size of  $\alpha$  precipitates between deformed conditions, ImageJ color thresholding was used to calculate size and distribution of particles. The calculations were done using the phase maps in **Figure 9b** and **Figure 9e**. Given the irregular shape of precipitates in Ti5553\_800C\_D001 condition, the size was calculated based on the area, not on the diameter of particles (for which an assumption of spherical particles would need to be made). **Figure 13** presents the plots of size distribution with the resulting weighted average size for each case. As expected from microstructure images, the average size of precipitates in Ti5553\_800C\_D001 is considerably larger than in Ti5553\_800C\_D1.

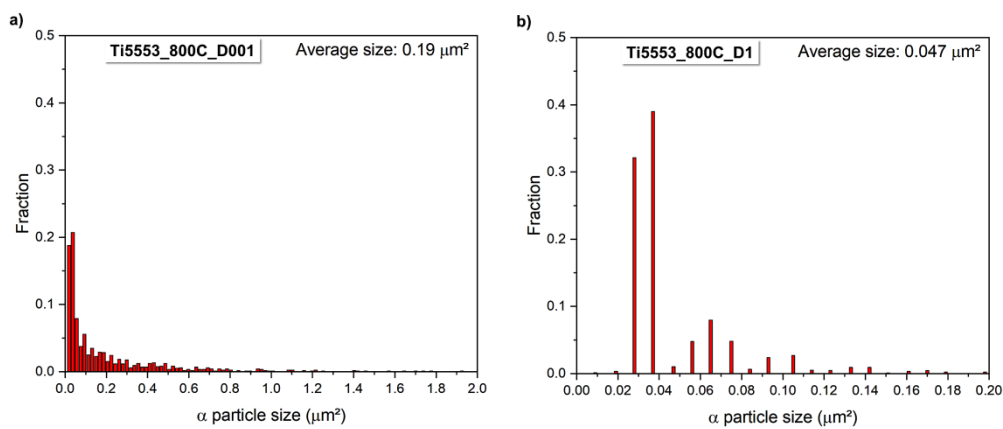


**Figure 13.** Size distribution of  $\alpha$  particles in **a)** Ti5553\_800C\_D001 and **b)** Ti5553\_800C\_D1 conditions.

In **Figure 14**, the misorientation distribution of  $\alpha$  phase can be observed. The distribution in the Ti5553\_900C\_HT condition is similar to what previously verified for strain-free  $\alpha$  phase in a quenched Ti-6Al-4V alloy [30,31]. The peaks at  $\sim 60^\circ$  and  $\sim 90^\circ$  correspond to different variants of the Burgers orientation relationship selected during the  $\beta \rightarrow \alpha$  transformation ( $60^\circ/[1\ 1\ \bar{2}\ 0]$ ;  $60.83^\circ/[\bar{1}.337\ \bar{1}\ 2.377\ 0.359]$ ;  $63.26^\circ/[\bar{1}\bar{0}\ 5\ 5\ \bar{3}]$ ;  $90^\circ/[1\ \bar{2}.38\ 1.38\ 0]$ ). In the deformed condition,  $\alpha$ 's misorientation behavior is remarkably different. However, in both cases a tendency is seen to follow the so called Mackenzie distribution [32], which is the theoretical misorientation distribution for a perfectly random polycrystal, i.e. without preferential orientation [33]. This tendency is significantly more evident in Ti5553\_800C\_D1 condition. These results are in good agreement with the pole figures in **Figure 6**, which show a weak  $\alpha$  texture. Also, misorientation results show that the more fragmented  $\alpha$  phase is, the more random its orientation becomes.

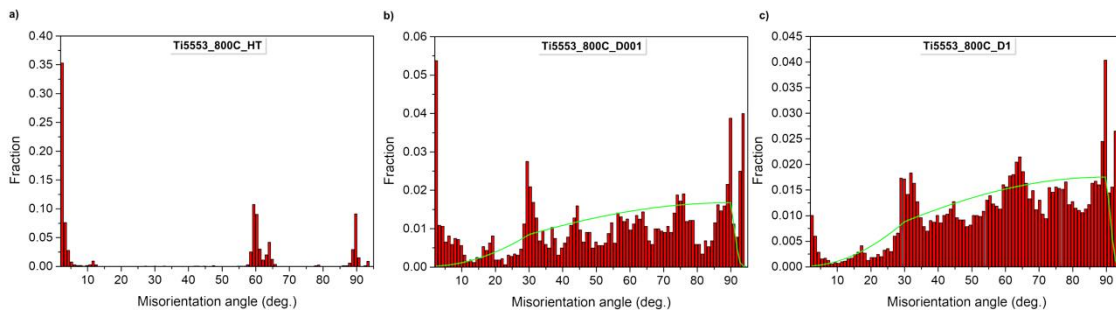


**Figure 14.** Misorientation distribution of  $\alpha$  phase in **a)** Ti5553\_800C\_HT, **b)** Ti5553\_800C\_D001 and **c)** Ti5553\_800C\_D1 conditions. The green curves are the corresponding Mackenzie (random) distributions.

High energy synchrotron X-ray diffraction data was used for phase quantification. Given the coarse microstructure, the possibility of running the experiment in transmission mode and the relatively large spot size enabled the acquisition of significant data volume from the bulk of samples. This makes phase quantification following this route more reliable with respect to EBSD, given the fact that  $\alpha$  is not homogeneously distributed and the probed area might not be representative enough. Diffractograms were integrated from the complete Debye-Scherrer rings acquired and **Figure 15** presents the resulting patterns for all conditions. In **Figure 15a**, the main  $\beta$  reflections are identified for clarification, and  $\alpha$  and  $\beta$  reflections are indicated in **Figure 15b**. In **Table 2** are shown the volume fractions obtained in all conditions produced at  $800^\circ\text{C}$  ( $R_{wp} \leq 0.1040$ ). An expressive difference between heat-treated and deformed conditions can be observed, in accordance with previously discussed results.

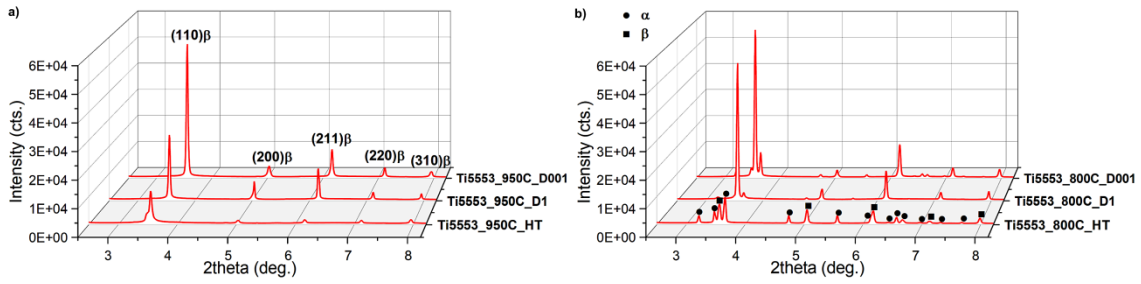


**Figure 15.** Resulting diffractograms of conditions produced at a) 950°C and b) 800°C with identification of  $\beta$  reflections and differentiation between  $\alpha$  and  $\beta$  reflections.

Condition	Ti5553_800C_HT	Ti5553_800C_D1	Ti5553_800C_D001
$\alpha$ fraction (%)	$67.4 \pm 0.7$	$8.4 \pm 0.6$	$24.3 \pm 0.5$

**Table 2.** Volume fractions of  $\alpha$  phase obtained for all conditions of Ti-5553 alloy at 800°C.

The average values of full width at half maximum (FWHM) and area of the three main  $\beta$  peaks, i.e. (110), (200) and (211) were measured ( $R^2 \geq 0.9578$ ). Results are shown in **Figure 16**. It is possible to observe that (110) $\beta$  and (211) $\beta$  follow the same tendency regardless of temperature: their areas and FWHM increase as strain rate decreases, and heat-treated conditions present the highest FWHM and lowest area values. However, (200) $\beta$  follows opposite tendencies: at 950°C, both FWHM and area increase with decreasing strain rate, while at 800°C the values of both parameters decrease. This can be correlated with results discussed above: dynamic recovery is associated with the formation of strong  $\langle 100 \rangle$  textures, but dynamic recovery dominance increases with increasing temperature and strain rate. Therefore, the behavior of (200) $\beta$  reflection is mostly affected, with the intensification of dynamic recovery causing a decrease in its FWHM and area.

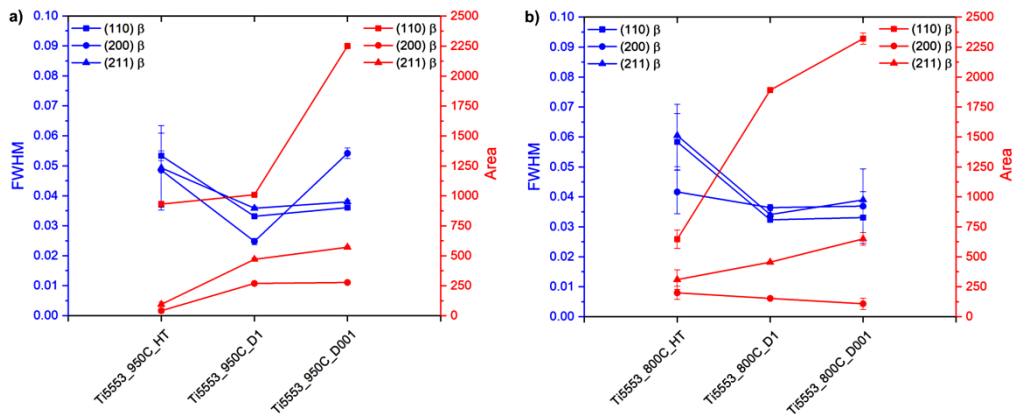


**Figure 16.** Average full width at half maximum (FWHM) and area evolution of (110) $\beta$ , (200) $\beta$  and (211) $\beta$  peaks for conditions produced at a) 950°C and b) 800°C.

## 5. Conclusions

The microstructure of  $\beta$ -metastable Ti-5Al-5Mo-5V-3Cr (Ti-5553) alloy after isothermal compression at 950°C ( $\beta$  field) and 800°C ( $\alpha+\beta$  field) with strain rates of  $10^{-1} \text{ s}^{-1}$  and  $10^{-3} \text{ s}^{-1}$  up to a compression ratio of 50% has been evaluated. From this study, the following conclusions can be drawn:

- $\beta$  undergoes dynamic recovery in all cases. Recovery is more dominant at lower strain rates in the  $\alpha+\beta$  field, as shown by the evolution of the phase's misorientation. In the single  $\beta$  field, misorientation analyses also imply that recovery is more dominant at lower strain rates, due to non-uniform deformation of grains during rapid deformation.
- During deformation in the  $\beta$  field with a higher strain rate, the occurrence of non-uniform recovery has been observed. This is critical to industrial processing, since the phenomenon causes a microstructural inhomogeneity that can affect mechanical properties of the alloy.
- When the alloy is deformed in the  $\alpha+\beta$  field,  $\alpha$  undergoes breakage and globularization during deformation. In addition, the amount of  $\alpha$  has varied significantly between heat-treated and deformed conditions, indicating that  $\alpha$  also decomposes during deformation.
- Upon deformation with higher strain rates,  $\alpha$  has shown itself to suffer a more intense globularization and refinement with respect to deformation at lower strain rates.
- Macrotecture evaluation has shown that only the texture of the  $\beta$  phase is significantly affected by deformation, more specifically the (200) component, whereas  $\alpha$  phase's texture presents itself relatively weak. This is in agreement with misorientation evaluation, since deformation causes a misorientation distribution which approaches the random distribution.

## Acknowledgements

The Materials Department of the Federal University of São Carlos (DEMa – UFSCar, São Carlos, Brazil) and the Brazilian Center for Research in Energy and Materials (CNPEM, Campinas, Brazil) are acknowledged for opening their facilities for the conduction of thermal and thermomechanical treatments. The *Deutsches Elektronen Synchrotron* (Hamburg, Germany) is acknowledged on the use of P07B beamline for the HEXRD experiments hereby presented. Sandvik Machining Solutions (Stockholm, Sweden) is also acknowledged for the provision of the studied material. JPO acknowledges Fundação

para a Ciência e a Tecnologia (FCT – MCTES) for its financial support via the project UID/EMS/00667/2019 (UNIDEMI).

### **Funding**

This work was supported by the National Council for Scientific and Technological Development – CNPq (grant number 161959/2015-6) and by the Coordination for the Improvement of Higher Education Personnel – CAPES (grant number 88887.302880/2018-00 and PROBRAL project 88881.143948/2017-01). Haroldo Pinto is CNPq fellow. The funding source had no involvement in the development of the research or in the preparation of the article.

### **Declaration of interest**

None.

### **Data availability**

The raw/processed data required to reproduce these findings cannot be shared at this time due to technical or time limitations.

### **References**

- [1] S.L. Nyakana, J.C. Fanning, R.R. Boyer, Quick reference guide for  $\beta$  titanium alloys in the 00s, *J. Mater. Eng. Perform.* 14 (2005) 799–811. doi:10.1361/105994905X75646.
- [2] J.C. Fanning, Properties of TIMETAL 555 (Ti-5Al-5Mo-5V-3Cr-0.6Fe), *J. Mater. Eng. Perform.* 14 (2005) 788–791. doi:10.1361/105994905X75628.
- [3] R.R. Boyer, R.D. Briggs, The use of  $\beta$  titanium alloys in the aerospace industry, *J. Mater. Eng. Perform.* 14 (2005) 680–684. doi:10.1007/s11665-013-0728-3.
- [4] J.C. Fanning, R.R. Boyer, Properties of TIMETAL 555 - a new near-beta titanium alloy for airframe components, in: *Proc. 10th World Conf. Titan.*, 2003: pp. 2643–2650.
- [5] N.G. Jones, R.J. Dashwood, D. Dye, M. Jackson, The flow behavior and microstructural evolution of Ti-5Al-5Mo-5V-3Cr during subtransus isothermal forging, *Metall. Mater. Trans. A.* 40 (2009) 1944–1954. doi:10.1007/s11661-009-9866-5.
- [6] N.G. Jones, M. Jackson, On mechanism of flow softening in Ti-5Al-5Mo-5V-3Cr, *Mater. Sci.*

- Technol. 27 (2010) 1025–1032. doi:10.1179/026708310x12668415533720.
- [7] H. Matsumoto, M. Kitamura, Y. Li, Y. Koizumi, A. Chiba, Hot forging characteristic of Ti-5Al-5V-5Mo-3Cr alloy with single metastable  $\beta$  microstructure, *Mater. Sci. Eng. A.* 611 (2014) 337–344. doi:10.1016/j.msea.2014.06.006.
- [8] M. Jackson, N.G. Jones, D. Dye, R.J. Dashwood, Effect of initial microstructure on plastic flow behaviour during isothermal forging of Ti-10V-2Fe-3Al, *Mater. Sci. Eng. A.* 501 (2009) 248–254. doi:10.1016/j.msea.2008.09.071.
- [9] M. Jackson, R. Dashwood, L. Christodoulou, H. Flower, The microstructural evolution of near beta alloy Ti-10V-2Fe-3Al during subtransus forging, *Metall. Mater. Trans. A.* 36 (2005) 1317–1327. doi:10.1007/s11661-005-0223-z.
- [10] M.C. Poletti, R. Buzolin, S. Kumar, P. Wang, T.F.J. Simonet-Fotso, Microstructure evolution of Ti-5Al-5V-5Mo-3Cr after hot deformation at large and moderate strains, *Mater. Sci. Forum.* 941 (2018) 1443–1449. doi:10.4028/www.scientific.net/MSF.941.1443.
- [11] J. Coakley, V.A. Vorontsov, N.G. Jones, A. Radecka, P.A.J. Bagot, K.C. Littrell, R.K. Heenan, F. Hu, A.P. Magyar, D.C. Bell, D. Dye, Precipitation processes in the Beta-Titanium alloy Ti-5Al-5Mo-5V-3Cr, *J. Alloys Compd.* 646 (2015) 946–953. doi:10.1016/j.jallcom.2015.05.251.
- [12] T. Furuhashi, T. Maki, Variant selection in heterogeneous nucleation on defects in diffusional phase transformation and precipitation, *Mater. Sci. Eng. A.* 312 (2001) 145–154. doi:10.1016/S0921-5093(00)01904-3.
- [13] R.P. Kolli, A. Devaraj, A review of metastable beta titanium alloys, *Metals (Basel)*. 8 (2018) 506–546. doi:10.3390/met8070506.
- [14] J.C. Teixeira, B. Appolaire, E. Aeby-Gautier, S. Denis, F. Bruneseaux, Modeling of the effect of the  $\beta$  phase deformation on the  $\alpha$  phase precipitation in near- $\beta$  titanium alloys, *Acta Mater.* 54 (2006) 4261–4271. doi:10.1016/j.actamat.2006.05.019.
- [15] J.C. Teixeira, B. Appolaire, E. Aeby-Gautier, S. Denis, L. Hélicher, Modeling of the phase transformations in near- $\beta$  titanium alloys during the cooling after forging, *Comput. Mater. Sci.* 42 (2008) 266–280. doi:10.1016/j.commatsci.2007.07.056.
- [16] F. Bachmann, R. Hielscher, H. Schaeben, Texture analysis with MTEX - Free and open source software toolbox, *Solid State Phenom.* 160 (2010) 63–68. doi:10.4028/www.scientific.net/ssp.160.63.

- [17] L. Lutterotti, S. Matthies, H.-R. Wenk, A.S. Schultz, J.W. Richardson, Combined texture and structure analysis of deformed limestone from time-of-flight neutron diffraction spectra, *J. Appl. Phys.* 81 (1997) 594. doi:10.1063/1.364220.
- [18] J.K. Fan, H.C. Kou, M.J. Lai, B. Tang, H. Chang, J.S. Li, Hot deformation mechanism and microstructure evolution of a new near  $\beta$  titanium alloy, *Mater. Sci. Eng. A.* 584 (2013) 121–132. doi:10.1016/j.msea.2013.07.019.
- [19] K. Li, P. Yang, The formation of strong  $\{100\}$  texture by dynamic strain-induced boundary migration in hot compressed Ti-5Al-5Mo-5V-1Cr-1Fe alloy, *Metals (Basel)*. 7 (2017) 1–8. doi:10.3390/met7100412.
- [20] K. Hua, J. Li, H. Kou, J. Fan, M. Sun, B. Tang, Phase precipitation behavior during isothermal deformation in  $\beta$ -quenched near beta titanium alloy Ti-7333, *J. Alloys Compd.* 671 (2016) 381–388. doi:10.1016/j.jallcom.2016.02.102.
- [21] M. Klimova, S. Zhrebtsov, G. Salishchev, S.L. Semiatin, Influence of deformation on the Burgers orientation relationship between the  $\alpha$  and  $\beta$  phases in Ti-5Al-5Mo-5V-1Cr-1Fe, *Mater. Sci. Eng. A.* 645 (2015) 292–297. doi:10.1016/j.msea.2015.08.008.
- [22] Q. Zhao, F. Yang, R. Torrens, L. Bolzoni, Comparison of hot deformation behaviour and microstructural evolution for Ti-5Al-5V-5Mo-3Cr alloys prepared by powder metallurgy and ingot metallurgy approaches, *Mater. Des.* 169 (2019) 107682(1–16). doi:10.3390/ma12030457.
- [23] S. Huang, Y. Ma, S. Zhang, S.S. Youssef, J. Qiu, H. Wang, B.Y. Zong, J. Lei, R. Yang, Nonuniform recrystallization and growth behavior of  $\beta$  grains dominated by grain misorientation and interfacial energy in metastable  $\beta$  titanium alloy, *Metall. Mater. Trans. A Phys. Metall. Mater. Sci.* 49 (2018) 6390–6400. doi:10.1007/s11661-018-4933-4.
- [24] X. Liu, D. Yu, Q. Fan, R. Shi, Influence of hot rolling and heat treatment on the microstructural evolution of  $\beta$ 20C titanium alloy, *Materials (Basel)*. 10 (2017) 1071. doi:10.3390/ma10091071.
- [25] T. Liu, L. Germain, J. Teixeira, E. Aeby-Gautier, N. Gey, Hierarchical criteria to promote fast and selective  $\alpha$ GB precipitation at  $\beta$  grain boundaries in  $\beta$ -metastable Ti-alloys, *Acta Mater.* 141 (2017) 97–108. doi:10.1016/j.actamat.2017.08.063.
- [26] X.G. Fan, Y. Zhang, P.F. Gao, Z.N. Lei, M. Zhan, Deformation behavior and microstructure evolution during hot working of a coarse-grained Ti-5Al-5Mo-5V-3Cr-1Zr titanium alloy in beta phase field, *Mater. Sci. Eng. A.* 694 (2017) 24–32. doi:10.1016/j.msea.2017.03.095.

- [27] N.G. Jones, R.J. Dashwood, D. Dye, M. Jackson, Thermomechanical processing of Ti-5Al-5Mo-5V-3Cr, *Mater. Sci. Eng. A*. 490 (2008) 369–377. doi:10.1016/j.msea.2008.01.055.
- [28] Q. Zhao, F. Yang, R. Torrens, L. Bolzoni, Effect of processing parameters on hot deformation behaviour and microstructural evolution of PM Ti-5553 alloy at a moderate-high strain rate, *Mater. Res.* 22 (2019). doi:10.1590/1980-5373-MR-2018-0738.
- [29] M. Dikovits, C. Poletti, F. Warchomicka, Deformation mechanisms in the near- $\beta$  titanium alloy Ti-55531, *Metall. Mater. Trans. A*. 45 (2014) 1586–1596. doi:10.1007/s11661-013-2073-4.
- [30] Q. Chao, P.D. Hodgson, H. Beladi, Ultrafine grain formation in a Ti-6Al-4V alloy by thermomechanical processing of a martensitic microstructure, *Metall. Mater. Trans. A*. 45 (2014) 2659–2671. doi:10.1007/s11661-014-2205-5.
- [31] H. Beladi, Q. Chao, G.S. Rohrer, Variant selection and intervariant crystallographic planes distribution in martensite in a Ti-6Al-4V alloy, *Acta Mater.* 80 (2014) 478–489. doi:10.1016/j.actamat.2014.06.064.
- [32] J.K. Mackenzie, Second paper on statistics associated with the random disorientation of cubes, *Biometrika*. 45 (1958) 229–240. doi:10.1093/biomet/45.1-2.229.
- [33] V. Randle, “Five-parameter” analysis of grain boundary networks by electron backscatter diffraction, *J. Microsc.* 222 (2006) 69–75. doi:10.1111/j.1365-2818.2006.01575.x.